Available online at www.sciencedirect.com
ScienceDirect
Engineering Fracture Mechanics 75 (2008) 3020–3037
Engineering Fracture Mechanics
www.elsevier.com/locate/engfracmech

Finite element modelling and analysis of crack shape evolution in mode-I fatigue Middle Cracked Tension specimens

R. Branco [a,*], F.V. Antunes [b]

[a] Department of Mechanical Engineering, Polytechnic Institute of Coimbra, 3030-129 Coimbra, Portugal
[b] Department of Mechanical Engineering, University of Coimbra, Pinhal de Marrocos, 3030-201 Coimbra, Portugal

Received 14 May 2007; received in revised form 11 December 2007; accepted 20 December 2007
Available online 31 December 2007

Abstract

A numerical procedure was employed to study the shape evolution of fatigue cracks in Middle Cracked Tension specimens. This iterative procedure consists of a 3D finite element analysis to obtain the displacement field in the cracked body, calculation of stress intensity factors along crack front and definition of local crack advances considering the Paris law. Numerical predictions were compared with experimental crack shapes with a good agreement. The evolution of crack shape was analysed for different propagation conditions considering robust dependent parameters. Two main propagation stages were identified: an initial transient stage highly dependent on initial crack shape and a stable stage where the crack follows preferred paths. Mathematical models were proposed for transient and stable stages consisting of exponential and polynomial functions, respectively. The transition between both stages was defined considering two criteria: the rate of shape variation and the distance to stable shape. Finally, the crack shape change was linked with the distribution of stress intensity factor along crack front.

Keywords: Crack shape evolution; MT specimen; Tunnelling parameter; Stress intensity factor

1. Introduction

In structures subjected to cyclic loads the designer may be needed to predict fatigue life. Modern damage-tolerant design approaches to fatigue are based on the assumption that engineering structures are inherently flawed, i.e., manufacturing defects are potentially present. Laboratory tests usually focus on ideal crack shapes (straight or elliptical), however for initially irregular cracks, interaction between cracks, etc., a significant portion of fatigue life can be spent in crack shape modification. Therefore, tools to predict crack shape evolution and fatigue life are required to improve life prediction.

* Corresponding author. Tel.: +351 239 790 700; fax: +351 239 790 701.
E-mail address: rbranco@isec.pt (R. Branco).

0013-7944/$ - see front matter © 2007 Elsevier Ltd. All rights reserved.
doi:10.1016/j.engfracmech.2007.12.012

Nomenclature

a_{av}	average crack length
a_T	propagation depth
b	surface angle parameter
c_1	constant of transient function
C, m	Paris law constants
B	specimen's thickness
dp	dependent parameter
d_{T1}, d_{T2}	transition depths
E	Young's modulus
FEM	finite element method
FCGR	fatigue crack growth rate
F_T, F_E	transient and stable functions
K	stress intensity factor
K_i	stress intensity factor of ith node
K_{min}, K_{max}, K_{av}	minimum, maximum and average stress intensity factors
L_1	radial size of crack front elements
MT	Middle Cracked Tension specimen
m	exponent of Paris law
N	number of load cycles
pt	tunnelling parameter
pt'	derivative of tunnelling parameter
q (q_i)	equilibrium distance (initial)
R	stress ratio
U	fraction of load cycle for which the crack remains fully open
W	specimen's width
W_E	work of external forces
x_c	rate of crack shape variation
x_1	transition limit of crack shape variation criterion
f_1	transition limit of transient function criterion
$\Delta a, \Delta a_{max}$	crack increment, maximum crack increment
ΔK	range of stress intensity factor
ΔK_{eff}	effective range of stress intensity factor
v	Poisson's ratio

Numerical techniques have been successfully employed to predict crack shape evolution and fatigue life. One of the most powerful approaches, widely quoted in literature for this purpose, consists of an iterative procedure based on a 3D FEM analysis. Firstly, a 3D finite element model is developed considering problem specificities, such as geometry, initial crack shape and size, loading and material properties. The displacement field is calculated in the cracked body and employed to predict the stress intensity factors along the crack front. Finally, nodal crack advances are defined using the Paris law, in order to create a new crack front. The whole procedure can be repeated up to final fracture, which occurs when maximum stress intensity factor reaches fracture toughness. Surface effects, such as crack closure or residual stresses, can be assessed considering different values of crack closure or of material properties along the crack front. In relation to the crack growth model two main methodologies can be distinguished. The simplest one, proposed by Newman and Raju [1,2] considers only few crack front keypoints (usually surface and deepest nodes), and assumes that a particular crack shape (circular, elliptical, etc.) is maintained during whole propagation. The crack can only change its aspect ratio. Although reasonable results are obtained [3,4], this approach cannot be applied to situations presenting significant shape variations during the crack growth. A more sophisticated methodology

was developed by Lin and Smith [5–7] considering several points along the crack front. This approach eliminates the crack shape constraint and was applied to planar cracks in fastener holes, to notched and unnotched round bars under tension, etc., by Lin and Smith [5–10]. Reliable predictions of crack shape evolution and stress intensity factors were also obtained by other authors. Couroneau and Royer [11,12] studied an edge flaw in a round bar under cyclic tension or bending loads; Gilchrist and Smith [13] studied short deep and long shallow semi-elliptical surface cracks under tension load; Nykänen [14] studied fatigue crack growth at the surface of a plate, and from the toe of a transverse non-load-bearing fillet weld in a T-joint; Lee and Lee [15] studied composite-repaired aluminium plates. Branco et al. [16] applied the technique to obtain the Paris law constants from regions with significant crack shape variation. Two experimental crack shapes were used along with the number of loading cycles between them.

According to several studies available in the literature, crack propagation exhibits two main stages [17–19]. Lin and Smith [6] studied three semi-elliptical surface cracks with different initial aspect ratios under tension and bending and concluded that, at the early propagation stage the shape change of each crack is different and strongly dependent on its initial aspect ratio. However, as these cracks propagate, they tend towards a preferred aspect ratio, reaching very similar profiles. Lazarus [17] analysed an embedded crack (elliptical or rectangular) in an infinite body loaded under mode-I and observed that after a certain time the crack becomes circular. Similar conclusions were presented in studies with cracks emanating from fastener holes and cracks in notched and unnotched round bars [9,10]. The cracks converge to shapes with constant fatigue crack growth along crack front and constant K (iso-K profile) [13]. However, there are initial crack geometries and loadings for which it is impossible to attain and maintain an iso-K profile [7].

In the literature, few efforts have been made to develop the mathematical modelling of the transient and stable propagation stages, and this will be the emphasis of this paper. A versatile automatic crack growth technique, based on 3D FEM with 9 nodes along crack front, was developed to study crack shape evolution in Middle Cracked Tension specimens with different initial cracks, specimen dimensions, linear elastic constants (E and v) and fatigue crack growth rates (C and m). The procedure was optimized and validated successfully with experimental results. It was applied to study the robustness of dependent parameters for crack shape characterization and to identify the main propagation stages. A mathematical model was proposed to predict the crack shape evolution during the whole propagation and fitted to the numerical results. Two transition criteria between the two main propagation stages were proposed and compared. Finally, the variation of crack shape was linked to the distribution of stress intensity factor along crack front.

2. Fatigue Middle Cracked Tension specimens: physical and numerical models

2.1. Physical model

Fig. 1a illustrates the MT specimen geometry studied, which is recommended in the standard ASTM E647. Fig. 1b exhibits the physical model considered in FEM analysis. Taking into consideration the symmetry of

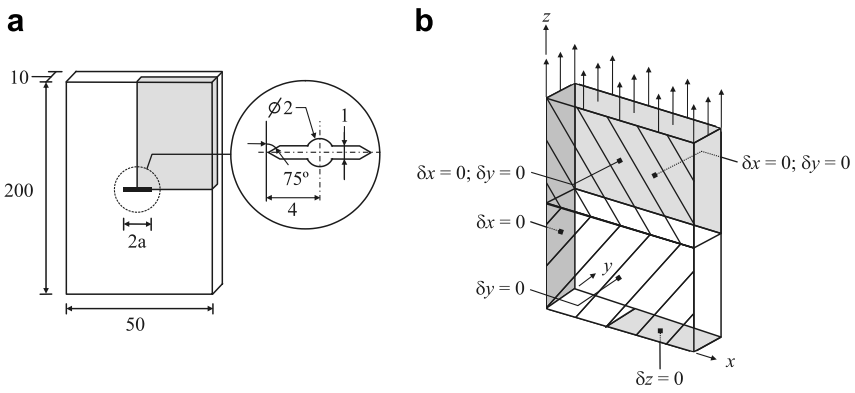

Fig. 1. (a) Middle Cracked Tension specimen geometry; (b) physical model.

geometry and loading, only one eighth of specimen was studied (grey volume of Fig. 1a), assuming adequate boundary conditions. The restrictions at the head of the specimen avoid rotation and bending, and intend to simulate the boundary conditions imposed by the rigid grips of the testing machine. The corner crack is planar, normal to the axis of the specimen and exists in its middle-section, therefore, mode-I loading exist along the whole crack front. The material was assumed to be homogeneous, isotropic and with linear elastic behaviour. A dynamic load with 5000 N of maximum load and $R = 0.1$ was applied, which imposes a maximum remote stress of 10 MPa.

2.2. FEM model

The numerical model was created using isoparametric hexahedric elements with 20 nodes (Fig. 2a), isoparametric pentahedric elements with 15 nodes (Fig. 2b) and singular pentahedric elements with nodes at quarter-point positions (Fig. 2c). A full Gauss integration was used for these elements, i.e., $3 \times 3 \times 3$ integration points for hexahedric elements and 21 integration points for pentahedric elements. The finite element mesh was defined with three different regions: a spider web mesh (Fig. 2e) made of concentric rings (Fig. 2d) centred on the crack front, a regular mesh region away from the crack front with relatively large elements (Fig. 2g) and a transition region (Fig. 2f) between those. Singular elements were considered at the crack front. The spider web mesh has 8 layers of elements along the thickness (Fig. 2e). In this paper, a uniform distribution of layers is considered. Similar analysis with non-uniform layers can be found elsewhere [20]. The transition mesh (Fig. 2f) connects the dense spider web mesh with the regular mesh, this having only 4 layers of elements along the thickness and a regular aspect. The assembled model is given in Fig. 2h. This mesh topology is able to accommodate different crack shapes and promotes a smooth change from a refined mesh near the crack front to a larger mesh at remote positions. The mesh has 4073 nodes and 1228 elements (116 pentahedric elements and 1112 hexahedric elements).

In the numerical study, several initial average crack lengths (2.5, 7.5 and 12.5 mm), specimen's thicknesses (2.4, 3, 4, 7.2, 10 mm) and initial crack shapes (straight, curved and chevron type) were studied. The crack front coordinates of the different cases are defined in Table 1, where x_i and y_i are the crack front coordinates measured in x- and y-directions (see Fig. 1b); a_{av} is the average crack length; B is the specimen's thickness; and d is defined in Fig. 5a.

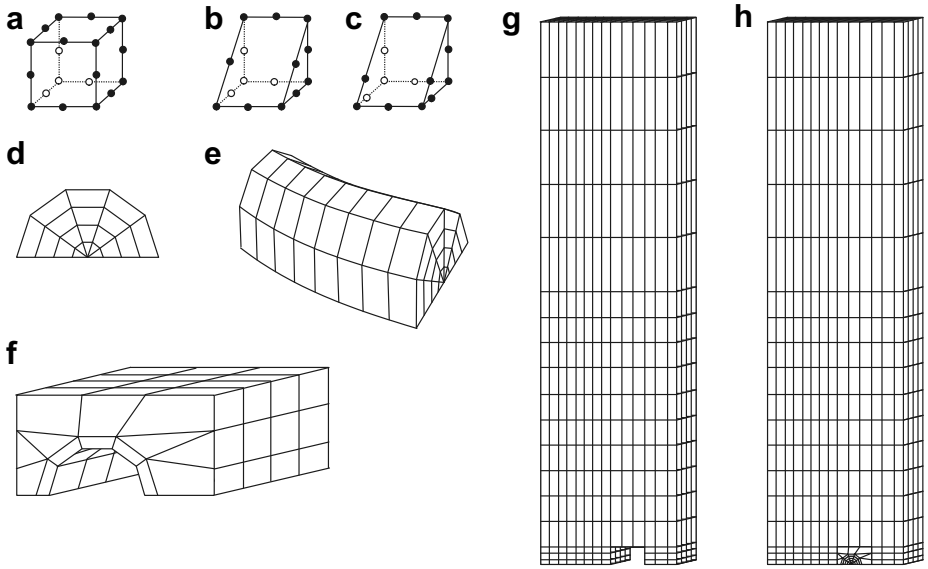

Fig. 2. (a) Isoparametric hexahedric elements with 20 nodes; (b) isoparametric pentahedric elements with 15 nodes; (c) singular pentahedric elements with nodes at quarter-point positions; (d) spider web pattern; (e) spider web mesh with uniform layers distribution; (f) transition mesh; (g) regular mesh; (h) assembled model.

Table 1
Relative nodal crack front coordinates of initial crack shapes (mm)

Node, i	Fraction of thickness, $2y_i/B$ (–)	Initial crack shape, x_i (mm)		
		Straight	Curved	Chevron
1	0.000	a_{av}	$a_{av} - 0.528$	$a_{av} - 4d/8$
2	0.125	a_{av}	$a_{av} - 0.428$	$a_{av} - 3d/8$
3	0.250	a_{av}	$a_{av} - 0.328$	$a_{av} - 2d/8$
4	0.375	a_{av}	$a_{av} - 0.228$	$a_{av} - d/8$
5	0.500	a_{av}	$a_{av} - 0.078$	a_{av}
6	0.625	a_{av}	$a_{av} + 0.072$	$a_{av} + d/8$
7	0.750	a_{av}	$a_{av} + 0.272$	$a_{av} + 2d/8$
8	0.875	a_{av}	$a_{av} + 0.472$	$a_{av} + 3d/8$
9	1.000	a_{av}	$a_{av} + 0.772$	$a_{av} + 4d/8$

2.3. Automatic crack growth technique

Fig. 3 illustrates the automatic crack growth technique employed in this study. This procedure can be divided into three main parts: pre-processing, processing (grey boxes) and post-processing. The first one is dedicated to define the geometry, boundary conditions, loading, initial crack shape and material properties (elastic constants and fatigue crack growth rate). The second one consists of three successive cyclic steps which are repeated up to the final fracture, or as long as necessary: finite element method generation, stress intensity factor calculation and crack growth model. The last step is the analysis of results in the post-processing stage.

The effect of this automatic procedure on the crack front is illustrated in Fig. 4. First, the finite element mesh is generated in order to calculate the displacement field (Fig. 4a). ModuleF, a non-commercial package was used to carry out this task. The displacement field is used to calculate mode-I stress intensity factor for each crack front node (Fig. 4b). Several alternative methods can be used to calculate the stress intensity factor along the crack front. An extrapolation method with 2 points was used in this study. The stress intensity factor was calculated at two points on the crack surface by

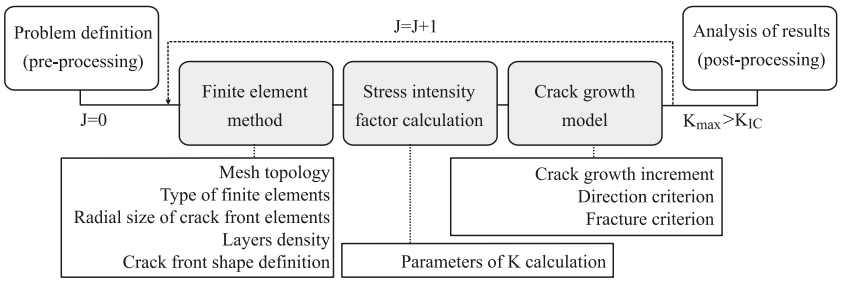

Fig. 3. Algorithm of the automatic crack growth technique.

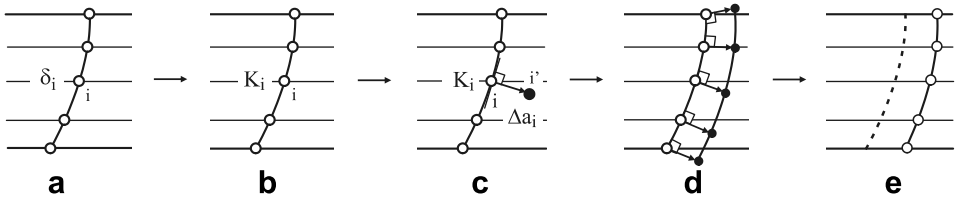

Fig. 4. Automatic crack growth technique: (a) initial crack front; (b) K calculation along crack front; (c) node displacement; (d) definition of new crack front; (e) final adjustments.

$$K = \sqrt{\frac{\pi}{8r}} \times \frac{E}{(1-v^2)} \times v_p \tag{1}$$

where v_p is the crack opening displacement, r is the radial distance from crack tip, E and v are the elastic constants assuming an isotropic behaviour.

The local crack increments are then obtained (Fig. 4c) using the K values previously calculated and the Paris law obtained experimentally:

$$\frac{da_i}{dN} = C(\Delta K_i)^m \tag{2}$$

where da_i/dN is the local crack growth rate and ΔK_i is the stress intensity factor range at an arbitrary point i along the crack front. The propagation at each crack front node, under remote mode-I loading, is assumed to occur along a normal direction to the crack front. The crack increment at an arbitrary node along the crack front can be derived from previous equation, and can be expressed as

$$\Delta a_i^{(j)} = \left[\frac{\Delta K_i^{(j)}}{\Delta K_{\max}^{(j)}}\right] \Delta a_{\max}^{(j)} \tag{3}$$

being $\Delta a_{\max}^{(j)}$ the maximum crack growth increment for jth iteration. In order to study the effect of crack closure on fatigue crack growth, an effective stress intensity range was considered, given as follows:

$$\Delta K_{i\text{eff}}^{(j)} = U_i \cdot \Delta K_i^{(j)} \tag{4}$$

where U_i is the fraction of the load cycle for which the crack remains fully open. Once ΔK varies with crack growth, Euler algorithm can be used to calculate the number of load cycles, leading to

$$N^{(j+1)} = N^{(j)} + \Delta N^{(j)} \Longleftrightarrow N^{(j+1)} = N^{(j)} + \frac{\Delta a_{\max}^{(j)}}{C[\Delta K_{\max}^{(j)}]^m} \tag{5}$$

Adding these displacements to the initial nodal coordinates, new nodal positions are defined and consequently, a new crack front is generated (Fig. 4d). Lastly, some adjustments on the crack front are required, as illustrated in Fig. 4e. Cubic spline functions are used to define the positions of mid-side nodes, improving the crack shape definition and therefore, the general accuracy [5]. A 2D spider web pattern (Fig. 4d) is centred on each new nodal position. The connection of 2D meshes gives the 3D spider web mesh presented in Fig. 4e. The transition mesh is flexible to accommodate either curved or straight crack shapes.

2.4. Dependent parameters for crack shape characterization

Two independent parameters, the tunnelling effect parameter ($pt = d/B$) and the surface angle ($b = tg^{-1}h/p$), were employed here to characterize the global and local crack shapes, respectively. These parameters are schematized in Fig. 5. The angle b (slope angle in the limit $h \to 0$) is probably adequate to study the influence of different numerical and physical parameters on the crack propagation. Alternative parameters can be found in literature [10,20]. Crack size was characterized by the average crack length, a_{av}, defined as the average of nodal crack lengths. As schematized in Fig. 5a, B indicates specimen's thickness.

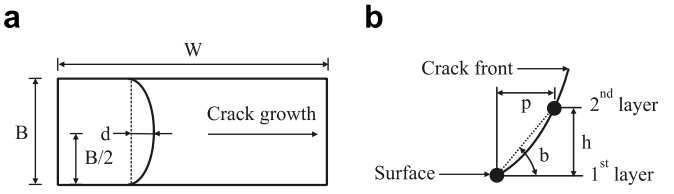

Fig. 5. Definition of crack shape parameters: (a) tunnelling effect; (b) surface angle.

2.5. Procedure optimization

The development of a feasible procedure to study crack shape evolution requires three main steps: model definition and implementation, identification of independent parameters affecting accuracy and optimization of these parameters. An effort was made to optimize the numerical procedure [20]. Several options were adopted initially, considering literature results and experience of the authors, namely the mesh topology consisting of a spider web mesh along crack front, the use of singular elements, the use of a cubic spline to define crack front and the use of a direct method for K calculation. However, other key aspects require a parametric study to define optimum values, namely the radial size of crack front elements, the layer distribution along crack front, the K calculation procedure and the maximum crack increment (Δa_{max}).

The optimized radial size of crack front elements (L_{1opt}) was defined maximizing the work of external forces (W_E). The optimum size of L_1 is independent of the crack size and crack shape, and was found to be $L_{1opt}/a_{av} = 4.2\%$, being a_{av} the average crack length. Values of L_1 larger than L_{1opt} are less problematic than smaller ones. The influence of different physical parameters on L_{1opt} was also studied. L_{1opt}/a_{av} was found to be influenced by specimen's thickness (B) and Poisson's ratio. The increase of v or B, decreases the optimum radial size. Multiple regressions were used to define a function relating these three variables, valid within $B \in [4\text{–}18]$ mm and $v \in [0.20\text{–}0.33]$

$$L_{1opt}/a_{av} = (0.10B^2 - 3.48B + 13.14)v^2 + (-0.06B^2 + 2.26B - 16.13)v + (0.009B^2 - 0.03B + 7.70) \quad (6)$$

The accuracy of the K calculation procedure was also studied. The direct method used showed errors lower than 2% for straight and curved cracked fronts. The maximum crack increment (Δa_{max}), Eq. (3), is also a main parameter of crack propagation procedure. The inaccuracy associated with Δa_{max} results from considering that $C(\Delta K)^m$ is constant within each propagation step, which is false since ΔK increases continuously. Reduction of Δa_{max} produces lower errors and there is a value below which this error can be neglected. Therefore, the objective is to obtain a reasonable value, which results in accuracy with a relatively low computational effort. Errors lower than 1% in dependent parameters were considered reasonable. In this study, the maximum crack increment was defined at each iteration as a fixed percentage of average crack length (a_{av}). Different initial crack shapes (straight and curved) and different values of $\Delta a_{max}/a_{av}$ (0.1% and12%) were considered. Fig. 6 presents the evolution of tunnelling parameter and surface angle for different values of $\Delta a_{max}/a_{av}$ and the percentage differences relatively to $\Delta a_{max}/a_{av} = 0.1\%$.

As exhibited in Fig. 6, an oscillatory tendency was observed for the relatively high values of $\Delta a_{max}/a_{av}$. This oscillatory tendency has been already reported in literature by several authors [8,20]. However, this behaviour decreases significantly when lower values of this parameter are adopted. The analysis of Fig. 6 indicates that

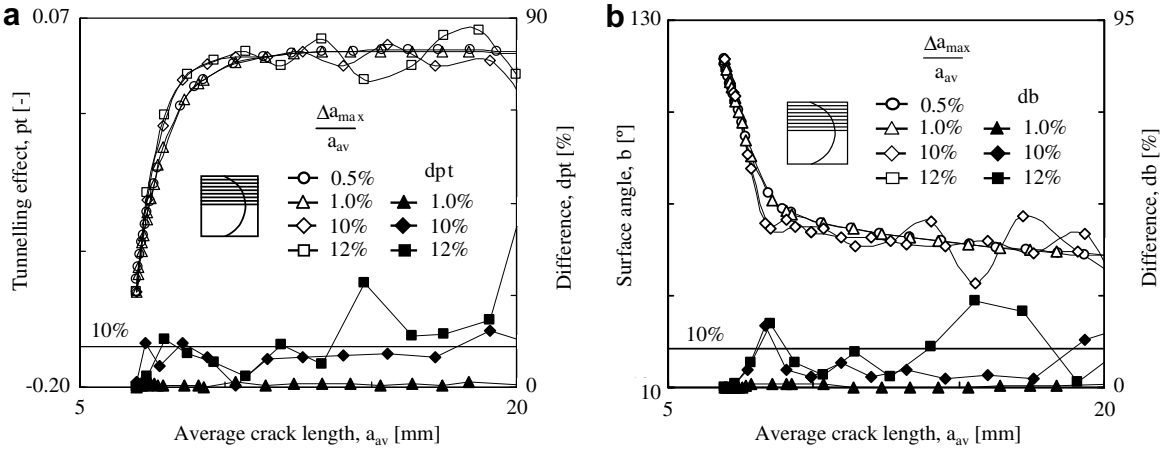

Fig. 6. Evolution of dependent parameters with a_{av} for different $\Delta a_{max}/a_{av}$: (a) *pt*; (b) *b*.

Table 2
Material properties of 6082-T6 aluminium alloy [21]

Fracture toughness, K_{IC}	20 MPa $m^{1/2}$
Tensile strength, σ	330 MPa
Young's modulus, E	74×10^3 MPa
Poisson's ratio, ν	0.33

Table 3
Paris law constants ($[da/dN]$ = mm/cycle; $[\Delta K]$ = MPa $m^{1/2}$) [21]

	C	m
$R = 0.25$	8.906×10^{-11}	3.456
$R = 0.10$	5.054×10^{-11}	3.554
$R = -0.25$	1.900×10^{-11}	3.978

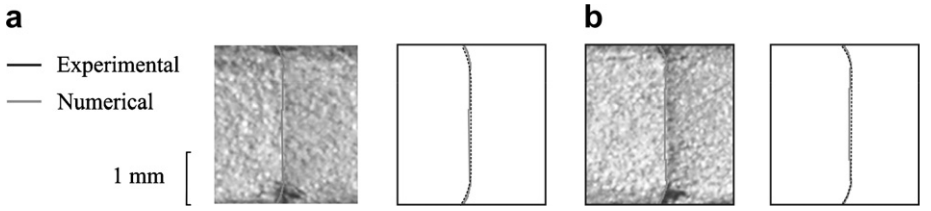

Fig. 7. Experimental validation: (a) $R = 0.25$ ($a = 11.76$ mm); (b) $R = -0.25$ ($a = 13.42$ mm).

considering $\Delta a_{max}/a_{av} = 1.0\%$ is enough to obtain errors lower than 1%. Therefore, this crack increment was adopted in subsequent work.

2.6. Experimental validation

The numerical predictions obtained were validated with experimental results. The experimental crack shapes were obtained by Borrego in crack closure studies [21] made in MT specimens according to the standard ASTM E647. Specimens with a fixed thickness of 3 mm were considered (the other dimensions are similar to the ones indicated in Fig. 1a). Table 2 presents main properties of 6082-T6 aluminium alloy. Tests were done at constant amplitude load for stress ratios of $R = 0.25$ and $R = -0.25$ (Paris law constants are presented in Table 3). Marking of crack fronts on fracture surface was done with overloads that duplicate maximum stress of load cycle.

Fig. 7a compares the experimental results for $R = 0.25$ and an average crack length of 11.76 mm, with numerical predictions. Fig. 7b compares crack shapes for an average crack length of 13.42 mm and a stress ratio $R = -0.25$. As can be seen, the results show a good agreement with the experimental results, which validates the numerical procedure.

3. Numerical results

3.1. Evolution of the crack shape

Fig. 8 exhibits the crack shape development in MT specimen for four different situations. Three different initial crack shapes were analysed: curved, chevron and irregular. These figures present only a limit number of crack shape profiles for improved clarity. U_1, U_2, U_3, indicate the closure levels at the first, second and third nodes from the free surface, respectively. The results in Fig. 8a and b show that crack closure delays the propagation near the free surfaces, i.e., produce some tunnelling, as could be expected. Comparison of Fig. 8c and d, indicate that, except for early propagation stage, the cracks tend towards a preferred aspect ratio, reaching a

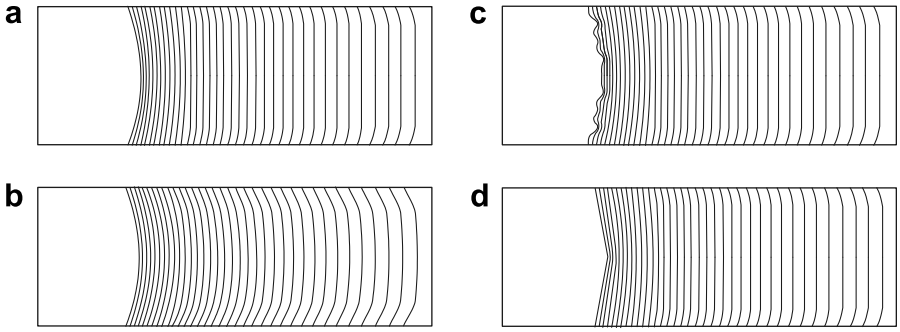

Fig. 8. Crack shape evolution ($B = 10$ mm, $v = 0.33$, $R = 0.1$, $C = 5.5054 \times 10^{-11}$; $m = 3.544$). Initial crack front: (a) curved; (b) curved with crack closure ($U_1 = 0.88$, $U_2 = 0.91$, $U_3 = 0.96$); (c) irregular front; (d) chevron.

very similar profile. During the early propagation stage, the shape change of each crack is different and strongly dependent on its initial aspect ratio. For a deeper analysis, the crack shape must be characterized using robust numerical parameters.

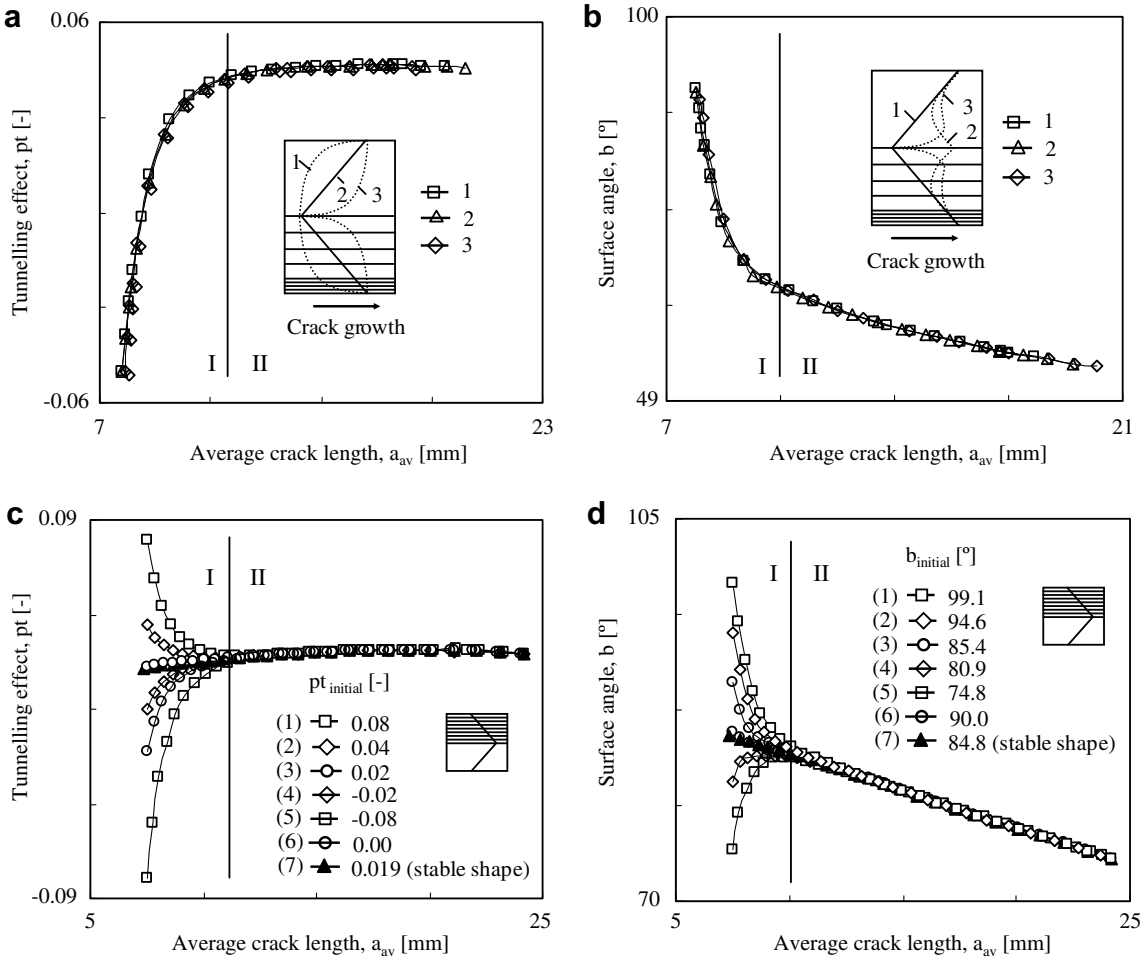

Fig. 9. (a) Evolution of *pt* for different cracks with the same initial value. (b) Evolution of *b* for different cracks with the same initial value. (c) Evolution of *pt* for different initial values. (d) Evolution of *b* for different initial values.

Fig. 9a and b shows the evolution of pt and b for three quite distinct initial crack shapes having all the same initial values of tunnelling effect ($pt = -0.05$) and surface angle ($b = 109.46°$). It can be observed that cracks having distinct initial shapes but the same initial values of dependent parameters follow similar paths during whole propagation. On the other hand, distinct propagations are obtained when the initial state of these parameters is different, as shown in Fig. 9c and d. Even cracks 3 and 7, although their similar initial values of pt and b, follow trajectories slightly different, proving the great impact of the initial crack shape on the crack propagation.

Fig. 9 also indicates that the crack propagation can be divided into two main stages [9–11,17–19]: an initial transient stage (I) highly dependent on the initial crack shape and with high crack shape variation gradients; and a subsequent stable stage (stage II) where the crack follows preferred paths which are not affected by the initial crack shape. Only one single path can be followed by the dependent parameters for each initial crack shape. This is an interesting conclusion since it establishes the possibility of a function relating initial parameters with crack shape evolution. However, cracks having different initial crack shapes can follow similar paths since they have the same initial values of dependent parameters. In general, the transient stage has a short dimension when compared with the stable stage. Nevertheless, the cracks that are initially more distinct from equilibrium shape take more time to reach that equilibrium. However, the crack tends always towards an equilibrium shape, independently on its initial remoteness.

3.2. Influence of different physical parameters

The development of a feasible mathematical model to predict the crack shape evolution needs a systematic identification of the physical variables affecting crack propagation. It was found that the crack shape evolution in this geometry depends on initial crack shape, crack length, specimen's thickness, Poisson's ratio, the Paris law exponent and level of crack closure. More details can be found elsewhere [20].

The effect of the initial crack shape is presented in Fig. 9. The effect of crack length can be also observed in Figs. 9 and 10. Fig. 10a shows the evolution of dependent parameters for three different values of the specimen's thickness (2.4, 4.0 and 7.2 mm) and three initial different crack lengths (2.5, 7.5 and 12.5 mm) without crack closure. The increase of the specimen's thickness decreases the tunnelling effect and increases the surface angle. This can be explained by the ratio of plane stress to plane strain regions, which decreases with thickness. In corner crack (CC) specimens [22] the degree of tunnelling seemed to be roughly twice as much as in CT specimens [23], also due to the extent of surface regions. The effect of CT specimen thickness on FCGR was studied at room temperature by Bao and McEvily [24] on 9Cr–1Mo steel and by Costa and Ferreira [25] on CK45 steel. They observed that the FCGR increases with that thickness, which was attributed to different levels of crack closure induced by plasticity. This level depends on plane strain to plane stress ratio regions, a quantity that increases with thickness.

The effect of Poisson's ratio (v) on the crack shape change is presented in Fig. 10b. Three different values ($0.25, 0.38, 0.45$) were studied along with three crack lengths (2.5, 7.5 and 12.5 mm). The results show the increase of Poisson's ratio increases the tunnelling effect. In fact, the portion of the crack front adjacent to a free surface has a loss of constraint to deformation. There is an almost general agreement that at corner points the singularity although existing is usually different from $r^{-0.5}$. The order of singularity depends on material's Poisson ratio, decreasing with this. Bazant and Estenssoro [26] determined a crack/surface angle that deviates from perpendicular in a manner consistent with subsurface crack advance and which strengthens the vertex singularity to 0.5. This critical angle (b_c) depends on loading mode and on v. For $v = 0.3$, b_c is 79.6° for mode-I and 113.0° for mixed mode II + III [27]. If $v = 0$, the singularity will also be $r^{-0.5}$ for all b. For mode-I loading, the increase of v reduces the critical angle, b_c [27], which is according the results of Fig. 10b. Heyder et al. have found a critical angle equal to 78.928° for rectangular cross-sections with $v = 0.3$ [28]. Fig. 11 compares values quoted in literature with the ones calculated in this study and an excellent agreement can be seen.

The effect of the exponent of the Paris law on crack shape evolution can be seen in Fig. 10c. Three values of m (1.155, 2.000 and 4.424) and three initial crack lengths (2.5, 7.5 and 12.5 mm) were analysed. The increase of m increases the tunnelling effect and decreases the surface angle. The effect of m is greater in early propagation stage, increasing the depth propagation needed to attain the stable phase. Lin and Smith

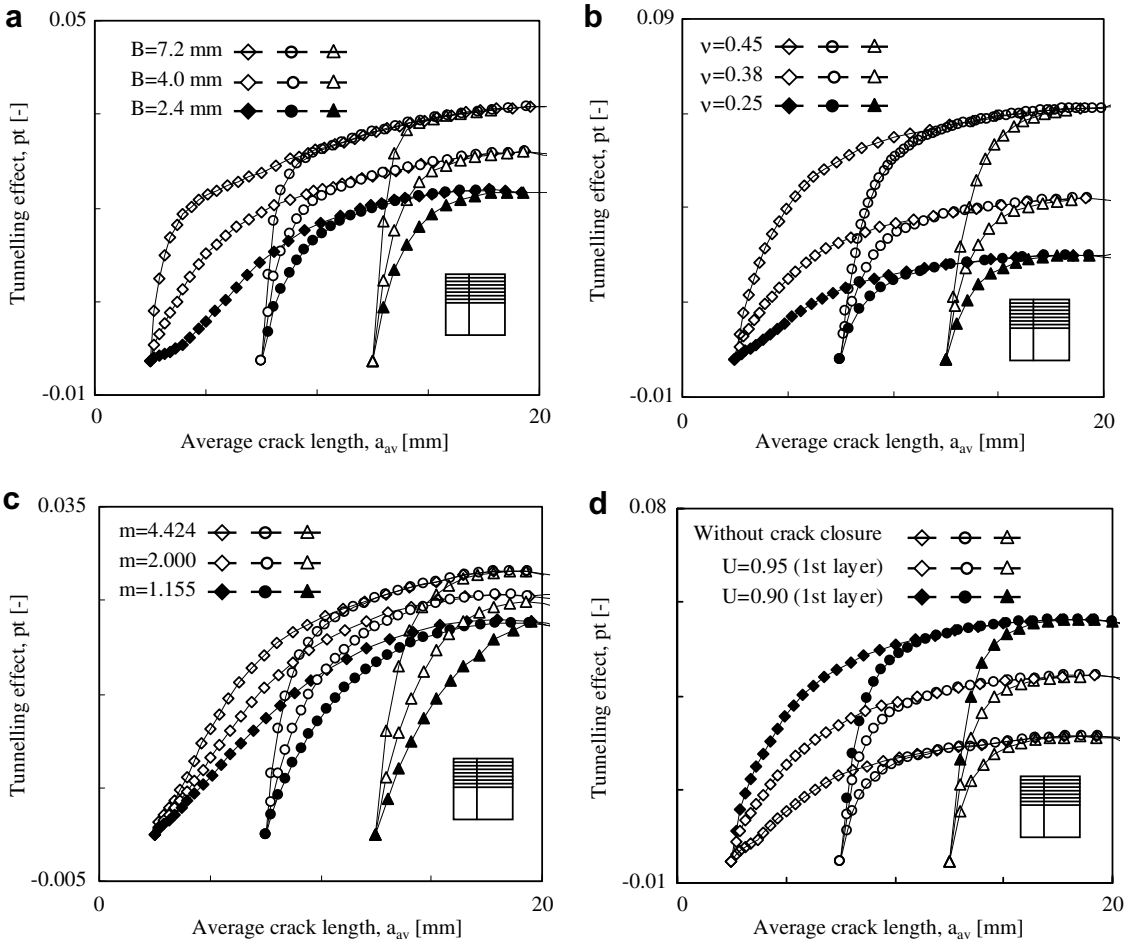

Fig. 10. Evolution of *pt* for three different values of: (a) specimen's thickness; (b) Poisson's ratio; (c) exponent of Paris law; (d) crack closure (reference values: $\nu = 0.33$, $m = 4.424$, $U = 1$, $B = 10$ mm).

[6] analysed fatigue crack growth of surface cracked plates and also demonstrated that larger values of *m* always make the aspect ratio change more intensely. This can be expected due to the power-law dependency of crack growth equation. On the other hand, stable propagation stages are less affected by this material

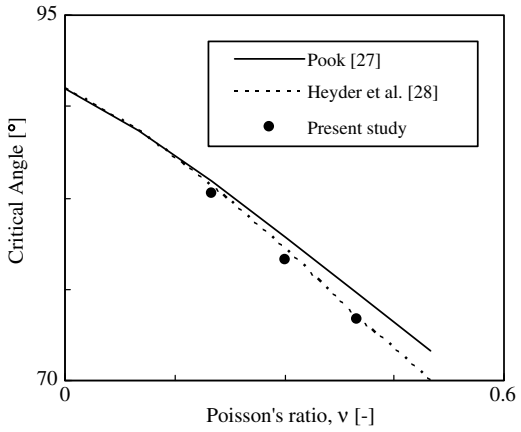

Fig. 11. Evolution of the critical angle with the Poisson's ratio.

parameter. In fact, the influence of m on the surface angle is irrelevant and on tunnelling effect is softer than previous properties analysed.

The crack closure is here used to describe the surface effect for crack propagation. The crack closure (U) effect was introduced on the propagation considering a reduction of stress intensity factor near the free surface, as described by Eq. (4). Fig. 10d shows the evolution of the dependent parameters for three closure conditions (without crack closure, $U_1 = 0.95$ and $U_1 = 0.90$) and three initial crack lengths (2.5, 7.5 and 12.5 mm). U_1 is the crack closure ratio at the surface node. The increase of U increases the tunnelling effect and decreases the surface angle, as was expected.

3.3. Mathematical modelling of propagation stages

The existence of a unique propagation path, as demonstrated previously, is an interesting conclusion as it permits the development of mathematical model suitable to predict the evolution of dependent parameters. The evolution of both dependent parameters (pt and b) can be characterized by the trajectory A to D shown in Fig. 12. The stable propagation is defined by BD curve, while the transient stage corresponds to AC. As mentioned earlier, the transient stage is usually relatively small portion compared with the stable one.

Let us consider that the stable propagation is known in whole domain. In practice, the path BD can be obtained considering an average crack length significantly lower than a_{av0}, or using an initial crack shape characterized by initial values of pt and b closer to the equilibrium shape (it means that A is very close to B). So, the evolution of either pt or b dependent parameters can be defined generically by the summation of two functions (see Eq. (7)): a stable function (F_E) and a transient function (F_T). Eq. (7) separates the variables affecting each part:

$$dp = F_E(m, v, B/W, U, a_{av}/W) + F_T(m, q_i, a_T/W) \tag{7}$$

where dp is either pt or b. The former exists permanently during whole propagation and quantifies the values of the dashed line BCD, presented in Fig. 12, while the latter has special importance during the earlier propagation stage and quantifies the difference between the generic dependent parameter evolution (ACD) and the corresponding stable dependent parameter evolution (BCD). In fact, it quantifies the evolution of q defined in Fig. 12. For the initial average crack length this difference is called q_i (initial value of q). As illustrated in Fig. 12, as the crack propagates, this difference tends toward zero and the transient function loses importance and can be ignored.

3.3.1. Transient function, F_T

The transient function can be calculated representing the evolution of absolute q with a_T. The latter is called propagation depth and is defined in Fig. 12 as the difference between the actual average crack length and the initial average crack length. Transient functions for the propagations presented in Fig. 9c (except curve 3), taking into account the stable propagation indicated in the same figure, are exhibited in Fig. 13a (notice that

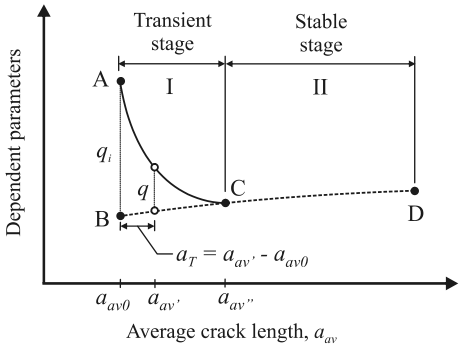

Fig. 12. Main concepts for mathematical modelling of transient and stable stages.

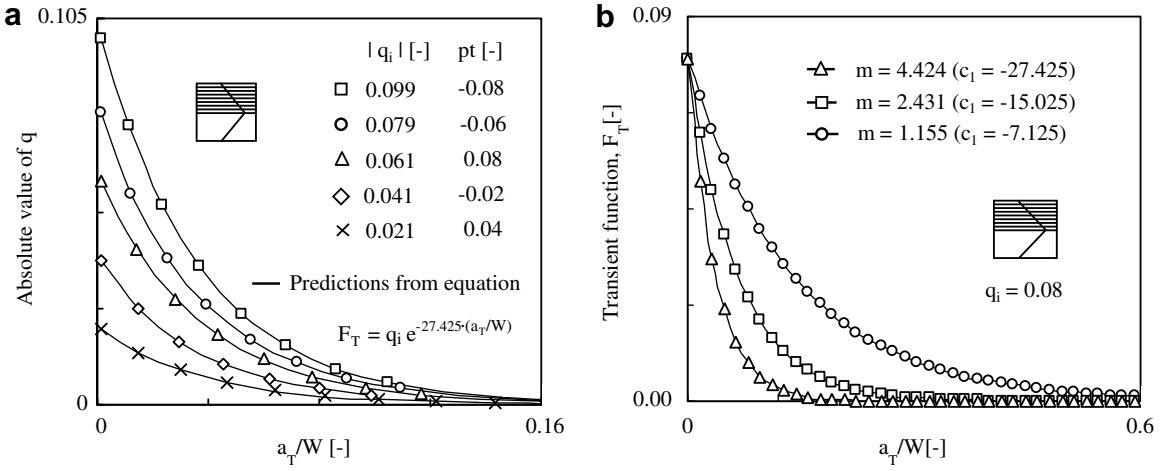

Fig. 13. Evolution of transient functions of *pt* for different values of: (a) q_i; (b) m.

curve 7 of Fig. 9c is the stable shape and was used to calculate the q values). It can be observed that the maximum value of each function occurs at the beginning of the propagation. As mentioned previously, this function tends towards zero as the crack grows. Furthermore, cracks with greater values of q_i, i.e., more distant from the equilibrium shape, take more time to approach zero.

These trends may be described using an exponential function as follows:

$$F_T = q_i e^{c_1 \cdot (a_T/W)} \tag{8}$$

For all the cases analysed in Fig. 13a, the value of c_1 is -27.425. A good agreement between numerical results (points) and equation predictions (lines) was obtained, with differences always lower than 2%. An individualised study of the effects of physical variables on c_1 constant was carried out and it was concluded that the value of this constant is a function of Paris law exponent. Fig. 13b exhibits the effect of three different values of m (4.424, 2.431 and 1.155) on F_T fixing q_i (0.08) and the initial average crack length (7.5 mm). Notice that Paris law exponent affects the crack propagation (as earlier mentioned in Fig. 10c) and consequently, for each value of this variable, a different stable crack shape can be distinguished. Thus, the three stable crack shapes were obtained previously and then the results of *pt* were used in order to define three adequate chevron crack shapes with the same average crack shape and the same value of q_i (it implies that three different initial chevron crack shapes were taken into account in this study). The points were fitted employing the generic expression 8 and each constant was calculated. It can be clearly observed that the effect of m cannot be ignored once it produces different curves and different c_1 constants as well. From Fig. 13b, it is possible to conclude that greater values of m cause smaller extensions of the transient function, that is, it tends towards zero more rapidly. Besides, the increase of the Paris law exponent increases the absolute value of the c_1 constant. For $m \in [1.155–4.424]$ and $B = 10$ mm, a general relationship between both variables (c_1 and m) was obtained by interpolation, and can be written as follows:

$$c_1 = -6.2109 \cdot m + 5.8094 \times 10^{-2} \tag{9}$$

A similar investigation was made for the surface angle, b, and similar trends were found for the transient function.

3.3.2. Stable function

The physical variables affecting stable crack propagation in MT geometry are the specimen's thickness, the Poisson's ratio, the exponent of the Paris law, the crack closure level and the average crack length. For a specific MT specimen geometry, initial crack and material, only a single path can be followed by the crack and

therefore, only a single stable function must be obtained (as illustrated in Fig. 12 by the dashed line). Consequently, for each set of initial conditions of the problem, it is only necessary to define a single function that gives the evolution of the dependent parameter with the average crack length. A fourth-order polynomial function fits adequately the trend obtained.

Taking into consideration the problem defined in Section 2 ($B = 10$ mm, $m = 4.424$, $v = 0.33$, $U = 1$), the stable function of pt (the one presented in Fig. 9a) with a square correlation equal to 0.999, can be written as follows:

$$F_E = -1.908 \times 10^{-1} \cdot \alpha^4 + 4.646 \times 10^{-1} \cdot \alpha^3 - 4.443 \times 10^{-1} \cdot \alpha^2 + 2.094 \times 10^{-1} \cdot \alpha - 1.442 \times 10^{-2} \quad (10)$$

where $\alpha = a_{av}/W$ and $\alpha \in [0.12–0.98]$. The stable function of the surface angle, as happened with the transient function, has a similar behaviour and can be fitted adequately with fourth-order polynomials. Branco [20] analysed comprehensively the influence of main physical variables on the evolution of both pt and b dependent parameters in MT specimen and proposed general equations for the intervals $m \in [1.155–4.424]$, $v \in [0.20–0.45]$, $B \in [4.0–20.0]$ mm and $U \in [1.0–0.90]$.

3.3.3. Transition depth

Beyond the modelling of both transient and stable functions it is also important to locate the transition between both stages (point C of Fig. 12). The transition depth (d_T) can be defined as the difference between the initial crack length and the length corresponding to $C(d_T = a_{av''} - a_{v0})$. Two criteria were used here to define the transition depth. The first criterion considers that the transition depth (d_{T1}) is reached when a predefined limit (x_l) of the rate of crack shape variation is attained. The rate of crack shape variation (x_c) can be calculated by differentiation of the transient function (Eq. (8)) in order to the propagation depth (a_T). This leads to

$$\frac{dF_T}{da_T} = c_1 q_i e^{c_1 a_T} \iff x_c = c_1 q_i e^{c_1 a_T} \quad (11)$$

Thus, the transition depth (d_{T1}) can be defined by the following equation:

$$c_1 q_i e^{c_1 d_{T1}} = x_l \iff d_{T1} = \frac{\mathrm{Ln}\left[\frac{x_l}{c_1 q_i}\right]}{c_1} \quad (12)$$

A transition depth based on the crack shape variation has also been defined by Couroneau and Royer [11]. The second criterion considers that the transition depth (d_{T2}) is reached when a predefined value of the transient function (f_l) is reached. It means that, the transition depth (d_{T2}) is given by

$$q_i e^{c_1 d_{T2}} = f_l \iff d_{T2} = \frac{\mathrm{Ln}\left[\frac{f_l}{q_i}\right]}{c_1} \quad (13)$$

Fig. 14a shows the relation between these two transition depths and the initial value of q (q_i) for the tunnelling effect parameter, taking into account the c_1 constant defined in Eq. (9) and assuming that x_l and f_l have the same absolute values, $|-5 \times 10^{-3}|$ mm^{-1} and $|-5 \times 10^{-3}|$, respectively. Three values of m, which affect directly the c_1 constant, were also studied, respectively 4.424, 2.424 and 1.155. Cracks relatively remote to equilibrium shapes, i.e., with relatively high q_i need more time to reach the equilibrium.

These two criteria can be compared assuming that the absolute values of x_l and f_l are similar:

$$|x_l| = |f_l| \iff |c_1 q_i e^{c_1 d_{T1}}| = |q_i e^{c_1 d_{T2}}| \iff d_{T1} = d_{T2} - \frac{\mathrm{Ln}[c_1]}{c_1} \quad (14)$$

By analysing the previous equation three conclusions can be made: if the absolute value of c_1 is greater than 1, then d_{T1} is greater than d_{T2}; if the absolute value of c_1 is lower than 1, then d_{T1} is lower than d_{T2}; and, finally, if the absolute value of c_1 is equal to 1, then d_{T1} is equal to d_{T2}. These conclusions are illustrated in Fig. 14 (where similar values x_l and f_l were taken into consideration). As can be seen, for example, for $c_1 = -27.425$ (corresponding to $m = 4.424$, as presented in Fig. 13b), the curves are almost coincident but actually d_{T1} is slightly greater than d_{T2}. For $c_1 = -15.025$ ($m = 2.431$), it is clearly distinguished that d_{T2} is

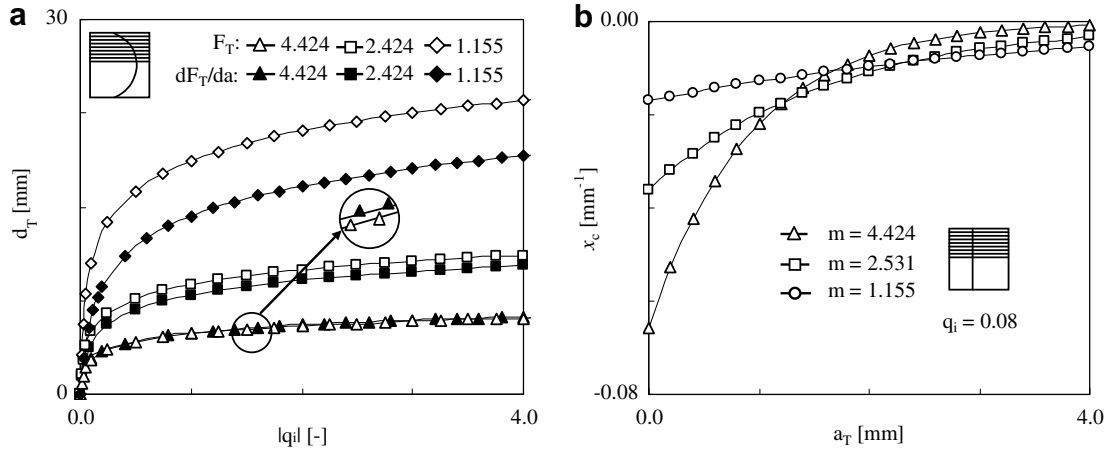

Fig. 14. (a) Comparison of transition depths obtained by both transition criteria; (b) influence of m on the rate of crack shape variation.

greater than d_{T1} in whole domain. For $c_1 = -7.125$ ($m = 1.155$), the inverse situation is observed. Similar conclusions can be made for the surface angle parameter.

Eq. (11) permits to estimate the evolution of the rate of crack shape variation. This rate, according to its definition, is dependent on the Paris law exponent. Fig. 14b presents the evolution of x_c for three different values of m. As can be seen, the curves tend asymptotically towards zero. The rate of crack shape variation rises with the Paris law exponent due to a higher driving force of crack shape. Several studies available in literature also concluded that higher values of m cause higher crack shape changes and that equilibrium is reached more quickly [6]. For $m = 4.424$ this rate is practically equal to zero when $a_T = 4$ mm. On the contrary, observing the evolution of x_c for the case with $m = 1.155$, it is expected that it approaches zero for a significantly higher value of a_T. Similar trends were obtained for x_c of b parameter.

3.4. Stress intensity factor distribution along the crack front

The distribution of stress intensity factor along crack front is the main driving force for crack shape modifications. On the other hand, each crack increment is accomplished by the modification of stress intensity factor distribution. Fig. 15a shows the evolution of K_{av}/K_{max} with a/W for an initial straight crack taking into account two set of properties ($m = 4.424$ and $\nu = 0.33$; $m = 1.155$ and $\nu = 0.20$), being K_{max} the maximum

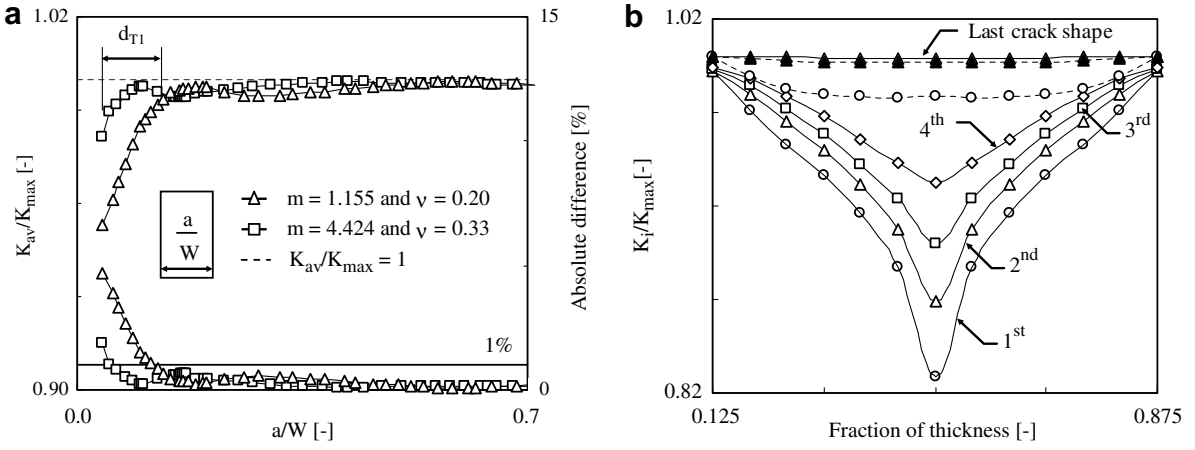

Fig. 15. (a) Evolution of K_{av}/K_{max} with a/W; (b) evolution of K_i/K_{max} distribution with a/W.

stress intensity factor for a given crack shape and K_{av} the average stress intensity factor. The absolute difference between K_{av}/K_{max} (in percentage) and $K_{av}/K_{max} = 1$ (dashed line) is presented at the bottom of the figure. In the early propagation region relatively high gradients of K were obtained, which are due to the great shape variations. A great influence of the Paris law exponent is observed in the earlier propagation stage. After this initial propagation period, this ratio converges towards unity and a clear stabilisation is exhibited. Fig. 15a also shows the transition depth obtained using Eq. (13) for $m = 4.424$ and $\nu = 0.33$. After this dimension (d_{T1}), the ratio is definitely stabilised which is a good indication that this criterion as a valid way to define the beginning of the stable region. In this propagation period, K_I values are quite stable and the differences between K_{av}/K_{max} and the unity are always lower than 1%.

Fig. 15b shows the distribution of K_i/K_{max} ratio along the fraction of thickness for the initial crack shape (chevron), the next three consecutive crack shapes and the final crack shape, being K_i the stress intensity factor of the ith node and K_{max} the maximum stress intensity factor. The distribution of ratio K_i/K_{max} for an initial straight crack shape and its corresponding final crack shape is given by the both dashed lines. Considerable K changes occur during the early crack propagation, forcing the crack towards a very similar K distribution independent of the initial crack shape. After the short initial propagation period, K_i/K_{max} is almost constant and equal to unity and the so-called iso-K profile is reached.

The next objective is to link the K distribution with the derivative function of pt (pt') as an attempt to relate the K variation (represented by K_{min}/K_{max}, where K_{min} is the minimum stress intensity factor) with the crack shape change (represented by pt'). Fig. 16 shows the evolution of pt' with the ratio K_{min}/K_{max} for different values of specimen's thickness, Poisson's ratio, Paris law exponent and crack length. This graphic exhibits a similar trend for all cases presented, which is a signal of an effective relationship between the K variation and the crack shape change. Three main regions are perfectly distinguished (notice that ordinate axis is presented on a logarithmic scale): an initial period with high values of pt'; a final period with expressive pt' reductions and almost constant K_{min}/K_{max} ratios; and an intermediate period with simultaneous variations of pt' and K_{min}/K_{max}. In the final period, pt' approaches zero which means that the crack is no longer changing its aspect ratio, i.e., the crack is in the stable region. On the contrary, in the initial period the crack changes strongly due a high driving force which leads it towards the equilibrium.

The effect of the Paris law exponent on pt' can be studied analysing the three filled series (square, circle and triangle). The increase of m, increases pt' (which means higher crack shape changes) but does not affect the initial ratio of K. Fig. 16 also compares the effect of the Poisson's ratio (filled and not filled squares) and it is possible to observe that the increase of this parameter, increases the value of pt' while the initial ratio of K_{min}/K_{max} decreases (in these cases the curves tends towards the same path). The effect of the specimen's thickness is given by the filled and not filled triangles: the initial value of K_{min}/K_{max} rises with the specimen's thickness, while the initial pt' drops.

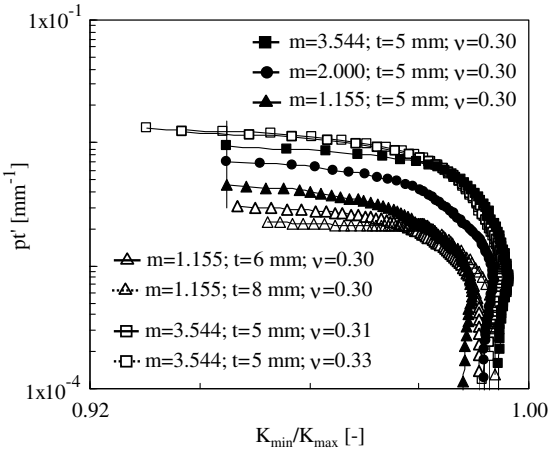

Fig. 16. Evolution of pt' with K_{min}/K_{max}.

4. Conclusions

An automatic technique based on the finite element method was developed to study 3D mode-I fatigue crack growth in MT specimens. The main conclusions of this study are:

- Main numerical parameters affecting the accuracy of automatic technique were identified and optimized. The maximum crack increment, Δa_{max}, is a main parameter and a value $\Delta a_{max}/a_{av}$ of 1.0% was found enough to obtain errors lower than 1%. The numerical predictions were compared with experimental crack shapes and a good agreement was observed.
- Two robust dependent parameters (tunnelling parameters and surface angle parameters) were proposed to characterize the crack shape evolution. The robustness of these parameters was demonstrated.
- Crack propagation can be divided into two main stages: a transient one that is quite dependent on initial crack shape and the Paris law exponent; and a stable one where the crack follows preferred paths. These preferred paths are a function of Poisson's ratio, exponent of Paris law, specimen's thickness and crack closure level.
- Mathematical models were developed for transient and stable stages, consisting of exponential and polynomial functions, respectively.
- The rate of crack shape variation was obtained by differentiation of transient function. The expression obtained shows that greater values of m drive the crack to attain crack shape variations close to zero more rapidly.
- Two transition criteria between propagation stages were proposed to estimate the transition depth extension. Cracks relatively far from equilibrium shapes need more propagation to reach equilibrium.
- A relationship was established between K distribution and crack shape variation. Three main regions were identified: an initial period with nearly constant values of pt' in logarithmic scale and important variations of K_i/K_{max}; an intermediate period characterized by more expressive reductions of pt' and lower variations of K_i/K_{max}; and a final period with values of K_i/K_{max} close to unity and significant reductions of pt'.

Acknowledgement

The authors acknowledge the financial support of FCT (Fundação para a Ciência e Tecnologia), through the project POCTI/EME/47022/2002.

References

[1] Newman Jr JC, Raju IS. An empirical stress intensity factor equation for the surface crack. Engng Fract Mech 1981;15:185–92.
[2] Newman Jr JC, Raju IS. Prediction of fatigue crack growth patterns and lives in three-dimensional cracked bodies. In: Sixth international conference on fracture, New Delhi, India, 4–10 December, 1984.
[3] Antunes FV, Ferreira JM, Costa JD, Capela C. Fatigue life predictions in polymer particle composites. Int J Fatigue 2002;24:1095–105.
[4] Burande S, Sethuraman R. Computational simulation of fatigue crack growth and demonstration of leak before break criterion. Int J Pressure Vessels Piping 1999;76:331–8.
[5] Lin XB, Smith RA. Finite element modelling of fatigue crack growth of surface cracked plates. Part I: the numerical technique. Engng Fract Mech 1999;63:503–22.
[6] Lin XB, Smith RA. Finite element modelling of fatigue crack growth of surface cracked plates. Part II: crack shape change. Engng Fract Mech 1999;63:523–40.
[7] Lin XB, Smith RA. Finite element modelling of fatigue crack growth of surface cracked plates. Part III: stress intensity factor and fatigue crack growth. Engng Fract Mech 1999;63:541–56.
[8] Lin XB, Smith RA. Shape evolution of surface cracks in fatigued round bars with a semicircular circumferential notch. Int J Fatigue 1999;21:965–73.
[9] Lin XB, Smith RA. Fatigue growth simulation for cracks in notched and unnotched round bars. Int J Mech Sci 1998;40:405–19.
[10] Lin XB, Smith RA. Fatigue shape analysis for corner cracks at fastener holes. Engng Fract Mech 1998;59:73–87.
[11] Couroneau N, Royer J. Simplified model for the fatigue crack growth analysis of surface cracks in round bars under mode I. Int J Fatigue 1998;20:711–8.

[12] Couroneau N, Royer J. Simplifying hypotheses for fatigue growth analysis of surface cracks in round bars under mode I. Comput Struct 2000;77:381–9.
[13] Gilchrist MD, Smith RA. Finite element modelling of fatigue crack shapes. Fatigue Fract Engng Mater Struct 1991;6:617–26.
[14] Nykänen TJ. Fatigue crack growth simulations based on free front shape development. Fatigue Fract Engng Mater Struct 1996;19:99–109.
[15] Lee WY, Lee JJ. Successive 3D analysis technique for characterization of fatigue crack growth behaviour in composite-repaired aluminum plate. Compos Struct 2004;66:513–20.
[16] Branco R, Antunes FJV, Martins Ferreira JA, Silva JM. Determination of Paris Law constants with a reverse engineering technique. In: 24th Spanish conference on fracture, Burgos, Spain, 21–23 Mars, 2007.
[17] Lazarus V. Brittle fracture and fatigue propagation paths of 3D plane cracks under uniform remote tensile loading. Int J Fract 2003;122:23–46.
[18] Favier E, Lazarus V, Leblond J. Coplanar propagation paths of 3D cracks in infinite bodies loaded in shear. Int J Solids Struct 2006;43:2091–109.
[19] Sukumar N, Chopp DL, Moran B. Extended finite element method and fast marching method for three-dimensional fatigue crack propagation. Engng Fract Mech 2003;70:29–48.
[20] Branco R. Numerical study of fatigue crack growth in MT specimens. MSc Thesis, Department of Mechanical Engineering, University of Coimbra, 2006 [in Portuguese].
[21] Borrego LPF. Fatigue crack growth under variable amplitude load in an AlMgSi alloy. PhD thesis, Department of Mechanical Engineering, University of Coimbra, 2001 [in Portuguese].
[22] Wanhill RJH. Significance of dwell cracking for IN718 turbine discs. Int J Fatigue 2002;24:545–55.
[23] Antunes FJV. Influence of frequency, stress ratio and stress state on fatigue crack growth in nickel base superalloys at elevated temperature. PhD thesis, Department of Mechanical and Manufacturing Engineering, University of Portsmouth, UK, 1999.
[24] Bao H, McEvily AJ. On plane stress–plane strain interactions in fatigue crack growth. Int J Fatigue 1998;20:441–8.
[25] Costa JDM, Ferreira JAM. Effect of stress ratio and specimen thickness on fatigue crack growth of CK45 steel. Appl Fract Mech 1998;30:65–73.
[26] Bazant ZP, Estenssoro LF. Surface singularity and crack propagation. Int J Solids Struct 1979;15:405–26.
[27] Pook LP. Some implications of corner point singularities. Engng Fract Mech 1994;48:367–78.
[28] Heyder M, Kolk K, Kuhn G. Numerical and experimental investigations of the influence of corner singularities on 3D fatigue crack propagation. Engng Fract Mech 2005;72:2095–105.